Analysis of Tilted Dipole Arrays: Impedance and Radiation Properties

Cristina Yepes, *Student Member, IEEE*, Erio Gandini, *Member, IEEE*, Stefania Monni, *Senior Member, IEEE*, Andrea Neto, *Fellow, IEEE*, Frank E. van Vliet, *Senior Member, IEEE*, and Daniele Cavallo, *Senior Member, IEEE*

***Abstract*— In this article, we investigate the radiation and impedance properties of arrays of tilted dipoles. A spectral periodic method of moments (MoM) is developed for the analysis of infinite arrays with arbitrarily tilted dipole elements, in free space or with a backing reflector. With the aid of this analysis method, the radiation characteristics of arrays of stacked dipoles over a ground plane are studied, explaining the variation of the patterns as a function of the interelement distance and the angle of inclination of the elements. Finite linear arrays of tilted dipoles are also investigated, to assess the dependence of the array characteristics on the number of elements. The developed method can be used to design arrays with nonsymmetric radiation patterns for angular filtering or pattern shaping.**

***Index Terms*— Antenna arrays, Floquet analysis, method of moments (MoM), pattern shaping.**

I. Introduction

ANTENNA arrays for satellite communication applications can be required to support very large scan angles, to be able to point to the satellites in any direction within a nearly hemispherical field of view. However, planar antenna arrays are typically characterized by scan loss, i.e., a reduction of gain when the beam is pointed at angles away from broadside. To increase the scan range, conformal arrays [1] or multipanel configurations [2] have been proposed, but the height of the structure is still too large to be installed on airplanes without significant impact on the aircraft drag.

To obtain wide-scan capability while still maintaining a low antenna profile, hybrid scanning methods have been implemented: the idea is to replace the typical planar array configuration, with symmetric field of view, with an array that scans the beam from broadside to a positive, as high as possible, angle. The full coverage is then achieved by mechanical rotation of the array along the azimuth.

An array of tilted stacked patches for digital video broadcast terminals was presented in [3], providing a 20°–70° coverage in elevation through electronic scan and 360° in azimuth through mechanical scan. The design choices were aimed at minimizing the number of active modules and, thus, the cost of the array. The asymmetric element pattern allowed reducing the amplitude of the grating lobes that appear due to an array spacing larger than half wavelength. However, with this configuration, the grating lobe level remains only 5.8 dB lower than that of the main lobe. Further attempts have been done to reduce the radiation toward undesired directions, while maintaining a large element spacing, e.g., in [4], by resorting to an overlapped beam-forming network. However, the improvement in terms of pattern selectivity is achieved at the cost of a more complex feeding architecture.

Although the mentioned works employed skewed antenna elements, the behavior of this type of arrays in terms of radiation characteristics has not been investigated in detail. The symmetry properties of arrays of antennas with asymmetric current distribution were studied in [5], based on a Floquet analysis. However, this analysis was only addressing the cases of planar antenna elements in infinite array environment. Here, we aim to extend the analysis to elements that can have vertical components in the current distribution, focusing also on interelement spacing exceeding half wavelength, and to study the asymmetric radiation properties of finite arrays.

For this purpose, we derive a periodic spectral method of moments (MoM) capable of modeling skewed dipoles. Analytical expressions are derived for the active input impedance of tilted dipoles, by assuming a single sinusoidal basis function to describe the current distribution. The active element patterns (AEPs) are also evaluated in closed form and a parametric analysis is then performed to show how the radiation patterns vary with the interelement distance and the inclination angle of the dipoles. The study provides useful design guidelines for tilted element arrays to achieve desired radiation characteristics.

Existing solutions for pattern shaping include amplitude and phase weighting of the elements [7]–[9] and density

Manuscript received March 28, 2019; revised July 26, 2019; accepted August 5, 2019. Date of publication September 9, 2019; date of current version January 3, 2020. This work was supported by the TNO Ph.D. Funding. *(Corresponding author: Cristina Yepes.)*

C. Yepes is with the Terahertz Sensing Group, Electrical Engineering, Mathematics and Computer Science Faculty, Delft University of Technology, 2628 CD Delft, The Netherlands, and also with the Department of Radar Technology, Netherlands Organization for Applied Scientific Research (TNO), 2597 AK The Hague, The Netherlands (e-mail: c.yepesjulia@tudelft.nl).

E. Gandini and S. Monni are with the Department of Radar Technology, Netherlands Organization for Applied Scientific Research (TNO), 2597 AK The Hague, The Netherlands.

A. Neto and D. Cavallo are with the Terahertz Sensing Group, Electrical Engineering, Mathematics and Computer Science Faculty, Delft University of Technology, 2628 CD Delft, The Netherlands.

F. E. van Vliet is with the Department of Radar Technology, Netherlands Organization for Applied Scientific Research (TNO), 2597 AK The Hague, The Netherlands, and also with the Center for Array Technology, University of Twente, 7522 NB Enschede, The Netherlands.

Color versions of one or more of the figures in this article are available online at http://ieeexplore.ieee.org.

Digital Object Identifier 10.1109/TAP.2019.2938838

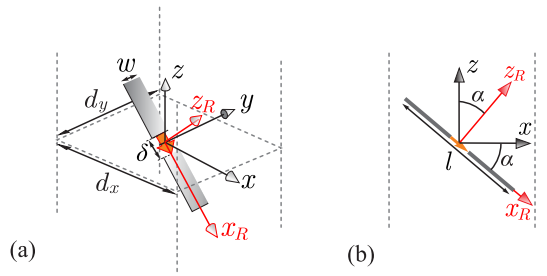

Fig. 1. Unit cell of an infinite array of tilted dipoles in free space with the original and rotated reference systems. (a) 3-D view. (b) Side view.

taper [10], [11]. Unlike these techniques, which require complex beam forming structures to independently control the amplitude and phase of each element, the method presented here only requires a linear progressive phase shift for scanning with no amplitude taper. Moreover, the synthesis procedure is very simple, mainly based on only two parameters: the interelement distance and the tilt angle of the elements. Element-level pattern diversity has also been used in [12] to combine different modes in the radiating elements as an additional degree of freedom. Similarly, here we exploit different Floquet modes within the array unit cell to achieve asymmetric patterns.

II. Periodic MoM for an Array of Skewed Dipoles in Free Space

To investigate the radiation properties of arrays of tilted elements, a periodic MoM solution is derived. For the sake of simplicity, we first consider an array of tilted strip dipoles in free space, as shown in Fig. 1. The dipoles are assumed to be tilted by an angle α with respect to the x-axis and excited with a delta gap source.

By applying the equivalence principle, unknown equivalent current densities radiating in free space can be defined on the dipole surface. The total current density for the infinite array can be written as a sum of doubly periodic contributions

$$\boldsymbol{j}_\infty(x,y,z)=\sum_{n_x=-\infty}^{\infty}\sum_{n_y=-\infty}^{\infty}\boldsymbol{j}(x-n_xd_x,y-n_yd_y,z)\cdot e^{-jk_{x0}n_xd_x}e^{-jk_{y0}n_yd_y} \quad (1)$$

where $k_{x0}=k_0\sin\theta\cos\phi$ and $k_{y0}=k_0\sin\theta\sin\phi$ are the x- and y-components of the wave vector associated with the scanning directions θ and ϕ, respectively, and k_0 is the free-space wavenumber at the calculation frequency.

The currents must satisfy the boundary conditions, that is, the tangential electric field vanishes on the metal ($\hat{z}_R\times\boldsymbol{e}_{\text{tot}}=0$), which is assumed to be perfect electric conductor (PEC). In the feeding gaps, the field is related to the current by the impedance boundary conditions ($\hat{z}_R\times\boldsymbol{e}_{\text{tot}}=Z_l\boldsymbol{j}$), where Z_l is an equivalent surface impedance related to the generator impedance of the feeds. Defining the function $\text{rect}_{\text{gap}}(\boldsymbol{r})$ to be 1 in the gap regions and zero elsewhere, we can write the electric field integral equation as

$$-\boldsymbol{e}_{\text{scat}}(\boldsymbol{r})+Z_l\boldsymbol{j}(\boldsymbol{r})\text{rect}_{\text{gap}}(\boldsymbol{r})=\boldsymbol{e}_{\text{inc}}(\boldsymbol{r}) \quad (2)$$

where we introduced the incident electric field $\boldsymbol{e}_{\text{inc}}=(V_0/\delta)\text{rect}_{\text{gap}}(\boldsymbol{r})$. The scattered field can be written in the space domain as a convolution integral

$$\boldsymbol{e}_{\text{scat}}(\boldsymbol{r})=\iiint_V\boldsymbol{j}_\infty(\boldsymbol{r}')\boldsymbol{g}(\boldsymbol{r},\boldsymbol{r}')d\boldsymbol{r}' \quad (3)$$

where $\boldsymbol{g}$ is the free-space dyadic Green's function, relating the electric field to the electric source, V is an infinite volume containing the entire dipole array, and $\boldsymbol{r}\equiv(x,y,z)$ and $\boldsymbol{r}'\equiv(x',y',z')$ are the observation and source points, respectively.

The scattered field can also be evaluated in the spectral domain, in terms of a double-Floquet modal expansion in x and y and an inverse Fourier integral for the z-variable

$$\boldsymbol{e}_{\text{scat}}(\boldsymbol{r})=\frac{1}{2\pi}\frac{1}{d_xd_y}\int_{-\infty}^{\infty}\sum_{m_x=-\infty}^{\infty}\sum_{m_y=-\infty}^{\infty}\boldsymbol{J}(k_{xm},k_{ym},k_z)\boldsymbol{G}(k_{xm},k_{ym},k_z)e^{-jk_{xm}x}e^{-jk_{ym}y}e^{-jk_zz}dk_z \quad (4)$$

where $\boldsymbol{J}$ is the 3-D Fourier transform of the current distribution in the unit cell with indexes $n_x=0$ and $n_y=0$, and $\boldsymbol{G}$ is the spectral dyadic Green's function, given in (34). The Floquet wavenumbers are $k_{xm}=k_{x0}-2\pi m_x/d_x$ and $k_{ym}=k_{y0}-2\pi m_y/d_y$, and k_z is the spectral counterpart of the spatial variable z.

The current density distribution on the dipole centered in the origin is assumed as a single entire-domain basis function:

$$j(x_R,y_R,z_R)\hat{\boldsymbol{x}}_R=i_0b_l(x_R)e(y_R)\delta(z_R)\hat{\boldsymbol{x}}_R \quad (5)$$

where we applied the separation of variables and we considered the rotated $(x_Ry_Rz_R)$-reference system, defined in Fig. 1. The coefficient i_0 is an unknown weight for the current distribution and $\hat{\boldsymbol{x}}_R$ is the unit vector aligned with the dipole axis. The chosen basis function comprises a longitudinal piecewise sinusoidal distribution [14]–[16]

$$b_l(x_R)=\frac{\sin(k_0(l/2-|x_R|))}{\sin(k_0l/2)} \quad (6)$$

where l indicates the dipole length, an edge-singular transverse profile [13]

$$e(y_R)=\frac{2}{\pi w}\left(1-\frac{2y_R}{w}\right)^{-1/2} \quad (7)$$

where w is the dipole width and a Dirac delta function $\delta(z_R)$, since the dipole thickness is assumed to be infinitesimal.

By applying the axis transformation

$$x_R=x\cos\alpha-z\sin\alpha,\qquad z_R=x\sin\alpha+z\cos\alpha \quad (8)$$

the current distribution can be expressed in the (xyz)-reference system (see Fig. 1) as

$$j(x,y,z)=i_0b_l(x\cos\alpha-z\sin\alpha)e(y)\delta(x\sin\alpha+z\cos\alpha). \quad (9)$$

As shown in Appendix A, the 3-D Fourier transform of the current can be derived as

$$J(k_x,k_y,k_z)=i_0J_0(k_yw/2)B_l(k_x\cos\alpha-k_z\sin\alpha) \quad (10)$$

where J_0 is the Bessel function of the zeroth order, representing the Fourier transform of the edge singular distribution, and B_l is the Fourier transform of the sinusoidal profile given by

$$B_l(k) = \frac{2k_0(\cos(kl/2) - \cos(k_0 l/2))}{(k_0^2 - k^2)\sin(k_0 l/2)}. \quad (11)$$

By applying the Galerkin method [17], we can define the active input impedance of the dipole as the projection (indicated as $\langle \cdot, \cdot \rangle$) of the field scattered by the basis function onto a test function, $\boldsymbol{t}$, chosen as equal to the basis function

$$Z_{\text{in}} = \frac{-\langle \hat{z}_R \times \boldsymbol{e}_{\text{scat}}(\boldsymbol{r}), \boldsymbol{t}(\boldsymbol{r}) \rangle}{i_0}. \quad (12)$$

By substituting (4) in (12), after some algebraic steps, the input impedance can be expressed in the spectral domain, for dipoles in free space, as follows:

$$Z_{\text{in,fs}} = \frac{-1}{2\pi d_x d_y} \sum_{m_x=-\infty}^{\infty} \sum_{m_y=-\infty}^{\infty} J_0^2\left(\frac{k_{ym} w}{2}\right) \int_{-\infty}^{\infty} B_l(k_{x_R}) B_l(-k_{x_R}) G_{x_R x_R}(k_{xm}, k_{ym}, k_z) dk_z \quad (13)$$

where $k_{x_R} = k_{xm}\cos\alpha - k_z \sin\alpha$ and $G_{x_R x_R}$ is related to xx-, xz-, and zz-components of the free-space dyadic Green's function by

$$G_{x_R x_R} = G_{xx}\cos^2\alpha - 2G_{xz}\sin\alpha\cos\alpha + G_{zz}\sin^2\alpha. \quad (14)$$

With the chosen sinusoidal basis function to represent the current on the dipole, the integrand in (13) can be written explicitly in closed form. The resulting expression presents a number of polar singularities, thus the integral can be solved analytically using the residue theorem, following the steps described in Appendix B.

For small electrical dimensions of the delta gap, the unknown coefficient i_0 can be found as $i_0 = V_0/(Z_l + Z_{\text{in}})$. Once the current i_0 is found, we can calculate the radiation pattern, by evaluating the expression in (4) only in the fundamental Floquet mode and calculating the integral in k_z with the residue theorem in the pole $k_{zm} = (k_0^2 - k_{xm}^2 - k_{ym}^2)^{1/2}$

$$\boldsymbol{e}(\boldsymbol{r}) = \frac{jk_{z0}}{d_x d_y} \frac{e^{-jk_0 r}}{2\pi r} \boldsymbol{J}(k_{x0}, k_{y0}, k_{z0}) \boldsymbol{G}_{2D}(k_{x0}, k_{y0}) \quad (15)$$

where $\boldsymbol{G}_{2D}(k_x, k_y)$ is the 2-D spectral dyadic Green's function in free space.

As a numerical example, we consider an array of dipoles of length $l = 0.5\lambda$, width $w = 0.1\lambda$, rotated by $\alpha = 30°$. The port impedance is set to $Z_l = 50\ \Omega$. The active input impedance and the AEP in the E-plane, calculated with the proposed method, are shown in Fig. 2 and compared with HFSS simulations, as a function of the scan angle. Two different periods are considered, $d_x = d_y = 0.5\lambda$ and $d_x = d_y = 0.6\lambda$. The discrepancy between the MoM and HFSS in terms of impedance is mainly due to the single basis function approximation we made for the current, which neglects the reactive energy stored in the feeding gap. However, the approximation is sufficient to properly represent the radiation patterns [Fig. 2(b) and (d)].

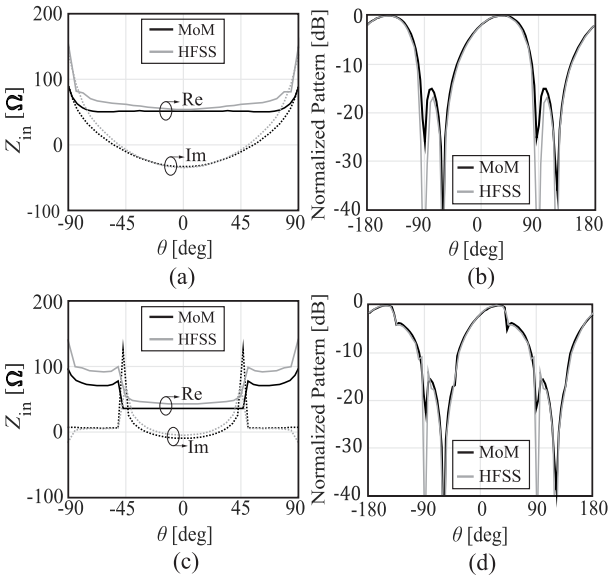

Fig. 2. Active input impedance for an infinite array of dipoles in free space with a spacing between elements of (a) 0.5λ and (c) 0.6λ. E-plane AEP for (b) 0.5λ and (d) 0.6λ. The dipoles are tilted 30° and the results of the MoM are compared with HFSS.

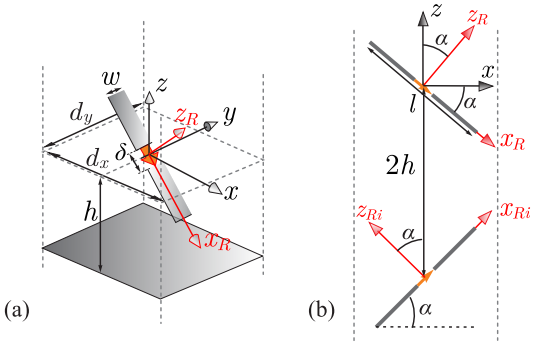

Fig. 3. Unit cell of an infinite array of tilted dipoles with a backing reflector. (a) 3-D view and (b) side view after applying the image theorem.

From the results shown in Fig. 2, it can be noted that the impedance is symmetric with respect to the scan angle, regardless of the periodicity. This result is consistent with the symmetry properties demonstrated in [5] for planar currents. A proof of the symmetry condition from the explicit expressions of the impedance is given in Appendix C, where we consider currents that can have vertical components. Despite the symmetry of the impedance, the AEPs are not symmetric with respect to the broadside direction, even for periods of 0.5λ. Therefore, tilted dipole elements in free space do not satisfy the pattern symmetry condition stated in [5]. For periodicity higher than half wavelength, discontinuities occur in the active input impedance and the AEP, due to grating lobes entering the visible region [18].

III. Dipoles With a Backing Reflector and Stacked Dipole Elements

A. Array of Dipoles With a Backing Reflector

We now consider tilted dipoles with their center at a distance h from a backing reflector, as depicted in Fig. 3(a). By applying the image theorem as in Fig. 3(b), the active

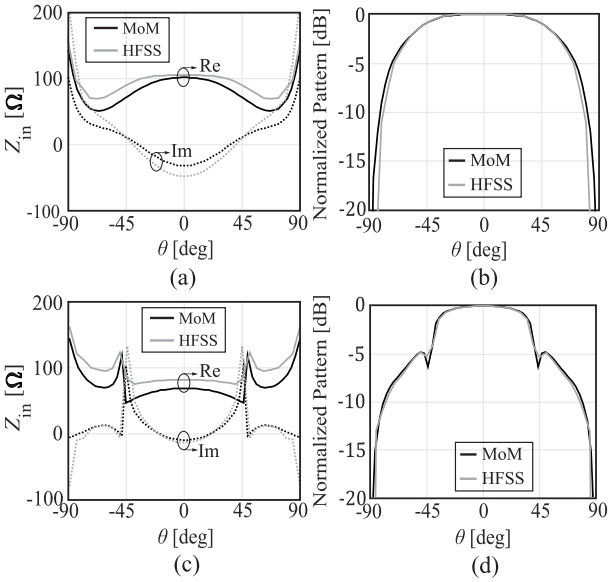

Fig. 4. Active input impedance for an infinite array of dipoles with a backing reflector, for (a) 0.5λ and (c) 0.6λ spacing. E-plane AEP for (b) 0.5λ and (d) 0.6λ. The dipoles are tilted 30° and the results of the MoM are compared with HFSS.

input impedance of the dipole can be written as the summation of the self-impedance and the mutual impedance with its image: $Z_{\text{in}} = Z_{\text{self}} + Z_{\text{mutual}}$, where Z_{self} coincides with $Z_{\text{in,fs}}$ in (13), whereas Z_{mutual} can be calculated in a similar way by including a shift $2h$ along the z-axis and an inverse tilt of the image compared to the main dipole

$$Z_{\text{mutual}} = \frac{-1}{2\pi d_x d_y} \sum_{m_x=-\infty}^{\infty} \sum_{m_y=-\infty}^{\infty} J_0^2\left(\frac{k_{ym} w}{2}\right) \int_{-\infty}^{\infty} B_l(k_{x_{Ri}}) B_l(-k_{x_R}) G_{x_R x_{Ri}}(k_{xm}, k_{ym}, k_z) e^{-jk_z 2h} dk_z \quad (16)$$

where $k_{x_{Ri}} = k_{xm}\cos\alpha + k_z \sin\alpha$ represents a wavenumber with inverse rotation compared to k_{x_R} and $G_{x_R x_{Ri}} = -G_{xx}\cos^2\alpha + G_{zz}\sin^2\alpha$. The radiated field is the summation of the field radiated by the dipole and by its image

$$\boldsymbol{e}(\boldsymbol{r}) = \frac{jk_{z0}}{d_x d_y} \frac{e^{-jk_0 r}}{2\pi r} \left(\boldsymbol{J}(k_{x0}, k_{y0}, k_{z0}) \pm \boldsymbol{J}_{\text{image}}(k_{x0}, k_{y0}, k_{z0})\right) \boldsymbol{G}(k_{x0}, k_{y0}) \quad (17)$$

where the "+" sign refers to the z-component of the currents and the "−" sign refers to the x-component of the currents, as a consequence of the image theorem. The image current spectrum $\boldsymbol{J}_{\text{image}}$ is given by

$$\boldsymbol{J}_{\text{image}}(k_x, k_y, k_z) = i_0 J_0(k_y w/2) B_l(k_x \cos\alpha + k_z \sin\alpha) \cdot e^{-jk_z 2h} \hat{\boldsymbol{x}}_{Ri}\,. \quad (18)$$

As numerical example, we consider the same dipole geometry as in Section II and we set $h = 0.25\lambda$. The active input impedance and the AEP for an interelement distance of 0.5λ and 0.6λ are plotted in Fig. 4, compared with HFSS.

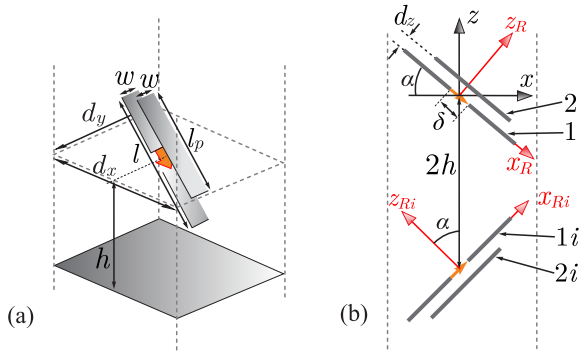

Fig. 5. Unit cell of an infinite array of tilted dipoles with a backing reflector. (a) 3-D view and (b) side view after applying the image theorem.

We can observe that the impedance is symmetric with respect to the scan angles, as for the free-space case. Regardless of the interelement distance, the AEP of an array of dipoles in the presence of a backing reflector is also symmetric with respect to broadside. This property can be explained with the fact that, as the dipole radiates the same power upward and downward, the power reflected by the ground plane is equal to the one radiated upward but in the specular direction. This result suggests using a more directive element to reduce the power reflected by the ground plane in the specular direction and to achieve asymmetry in the radiation.

B. Array of Stacked Dipoles With a Backing Reflector

In this section, we study stacked dipoles in the presence of a backing reflector, as depicted in Fig. 5(a). The unit cell consists of an active dipole with a parasitic strip to increase its directivity. The current distribution of the parasitic dipole, with length l_p, is given by

$$J_p(k_x, k_y, k_z) = i_p J_0(k_y w/2) B_{l_p}(k_x \cos\alpha - k_z \sin\alpha) \cdot e^{jk_x d_z \sin\alpha} e^{jk_z d_z \cos\alpha} \quad (19)$$

where i_p is an unknown amplitude. To simplify the notation, we number the basis functions with the indexes 1, 2 for the real dipoles and $1i$, $2i$ for their image, as shown in Fig. 5(b). The unknown weights for the currents on the active and passive dipoles (i_0 and i_p, respectively) can be found as

$$\begin{bmatrix} i_0 \\ i_p \end{bmatrix} = \left(\begin{bmatrix} Z_l & 0 \\ 0 & 0 \end{bmatrix} + \begin{bmatrix} Z_{1,1}+Z_{1,1i} & Z_{1,2}+Z_{1,2i} \\ Z_{2,1}+Z_{2,1i} & Z_{2,2}+Z_{2,2i} \end{bmatrix} \right)^{-1} \cdot \begin{bmatrix} V_0 \\ 0 \end{bmatrix} \quad (20)$$

where the self-impedance and mutual impedance terms can be expressed very similar to (13) and (16), by selecting the correspondent tilt and location of the basis functions. As an example, the geometrical parameters of the stacked dipole are set to $l = 0.5\lambda$, $l_p = 0.42\lambda$, $d_z = 0.07\lambda$, $w = 0.12\lambda$, and $\delta = 0.1\lambda$, where λ is the wavelength at the calculation frequency. These dimensions are selected to increase the directivity, compared to a single dipole.

Fig. 6 shows the input impedance and the AEP for scanning in the E-plane, for the stacked dipole element tilted by $\alpha = 30°$, at distance $h = 0.25\lambda$ from the ground plane, and for interelement distance of 0.5λ and 0.6λ. The input impedance for both interelement distances is again symmetric, as expected. A larger discrepancy between the method

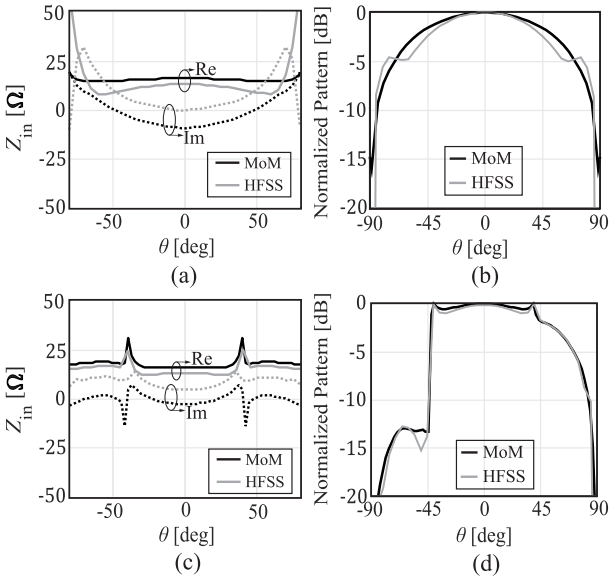

Fig. 6. Active input impedance for an infinite array of stacked dipoles with a backing reflector, for (a) 0.5λ and (c) 0.6λ spacing. E-plane AEP for (b) 0.5λ and (d) 0.6λ. The dipoles are tilted 30° and the results of the MoM are compared with HFSS.

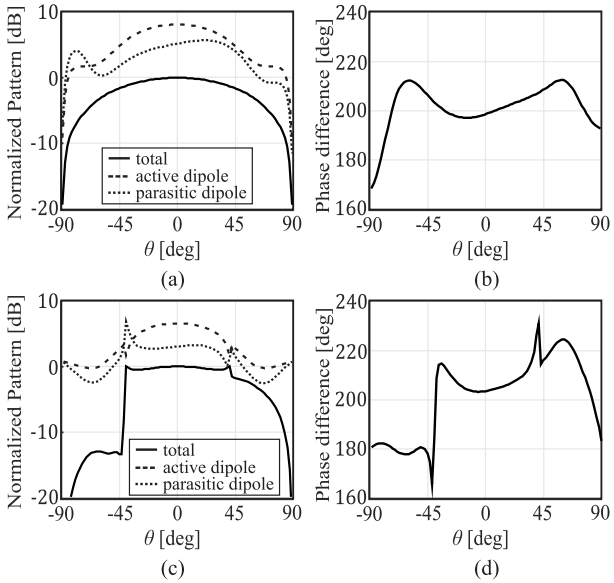

Fig. 7. AEP of array of tilted stacked dipoles with a backing reflector tilted by $\alpha = 30°$, with separate contribution from active dipoles and parasitic ones. (a) $d_x = d_y = 0.5\lambda$ and (c) $d_x = d_y = 0.6\lambda$. Phase difference between fields radiated by active and passive dipoles. (b) $d_x = d_y = 0.5\lambda$ and (d) $d_x = d_y = 0.6\lambda$.

described in this article and HFSS can be observed in the input reactance and in the pattern for $d_x = 0.5\lambda$, mainly due to the fact that the dipoles in the unit cells are very close to each other and therefore, an entire-domain sinusoidal profile is not accurate enough to represent the current distribution of both dipoles and the coupling between neighboring elements. Nevertheless, the radiation patterns calculated with our method still show a fair agreement with HFSS.

As it can be seen in Fig. 6, the radiated pattern is symmetric for 0.5λ period, whereas it is nonsymmetric for larger interelement distances. Thus, by comparing the results in Figs. 6(d) and 4(d), it can be noted that the increased directivity is a key property to realize nonsymmetric patterns. The steep gain drop that can be observed in Fig. 6(d) at around $\theta_{\text{drop}} = -42°$ corresponds to the angle at which a grating lobe enters in the visible region, that is,

$$\theta_{\text{drop}} = \sin^{-1}(1 - \lambda/d_x)\,. \tag{21}$$

The asymmetry can be further highlighted by analyzing the different contributions to the pattern from the active and parasitic dipoles. Fig. 7(a) and (c) report the separate contributions to the radiated field from the active and the passive dipoles, for array period of 0.5λ and 0.6λ, respectively. The radiated field of the stacked dipole is $\boldsymbol{e}_{total}(\boldsymbol{r}) = \boldsymbol{e}_d(\boldsymbol{r}) + \boldsymbol{e}_p(\boldsymbol{r})$, where $\boldsymbol{e}_d(\boldsymbol{r})$ is the field radiated by the active dipole and its image, calculated as in (17), while $\boldsymbol{e}_p(\boldsymbol{r})$ is the field radiated by the passive dipole and its image.

Both fields are normalized to the maximum of the total pattern, also shown in the figure. It can be observed that the amplitudes of the individual contributions are higher than their sum, which implies a partial cancellation of the radiated fields from two elements. This is also confirmed in Fig. 7(b) and (d), where the phase difference between the two radiated electric fields from active and parasitic dipoles is between 160° and 230°. Such values are also typical of superdirective arrays [19], [20], where higher directivity is obtained with arrays of closely spaced elements, that have very large and oppositely directed currents. It is important to remark that such configurations can lead to high Ohmic losses in realistic designs, due to the high current intensity. Nevertheless, efficiency aspects are not addressed in this article, as we only assume PEC as metal.

From Fig. 7(a), it appears that, although the pattern due to the passive dipoles is nonsymmetric, when summing the fields radiated by the active and passive dipoles, perfect symmetry is restored in the total pattern. This can be interpreted by noting that, since the period is 0.5λ, only a single radiating Floquet mode is supported by the structure. The aperture field due to this mode tends to be uniform in amplitude in the unit cell, providing a wide and symmetric radiation pattern. For a period of 0.6λ in Fig. 7(c), a high-order Floquet wave enters the visible region, thus the field distribution on the unit cell aperture supports an additional mode associated with radiation toward a different direction. Under this condition, the currents on the active and passive dipoles can produce cancellations that suppress the gain in certain angular regions. Indeed, the phase difference between the field radiated by the active and passive dipoles in Fig. 7(d) is close to 180° for angles between −90° and −45°.

C. Parametric Analysis

A parametric analysis on the radiation pattern of the tilted stacked dipole array is carried out to determine the parameters that affect the power radiated in specific directions. The considered geometrical variables are the interelement spacing (d_x, d_y) and the inclination angle of the dipoles (α). Fig. 8(a) and (b) shows the AEPs when varying the interelement distance and the tilt angle, respectively. All patterns are normalized to the broadside value for the maximum unit

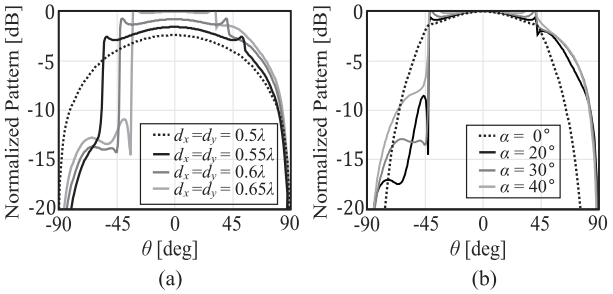

Fig. 8. AEP for an infinite array of stacked dipoles (a) tilted 30° for different spacings d_x, d_y and (b) with an interelement distance of 0.6λ for different tilt angles α.

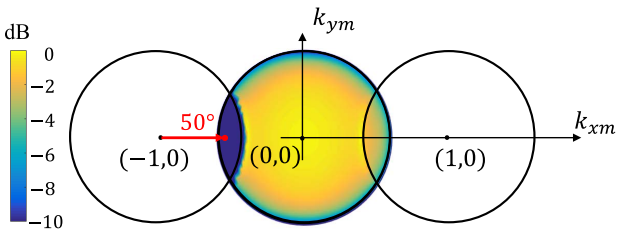

Fig. 9. Grating lobe diagram for a stacked dipole array with interelement distance of 0.6λ, tilted by $\alpha = 30°$. The grating lobe circles correspondent to the Floquet modes (m_x, m_y) equal to $(-1, 0)$, $(0, 0)$, and $(0, 1)$ are represented and the AEP is mapped in the visible region.

cell size, i.e., $d_x = d_y = 0.65\lambda$. Due to the relation in (21), the array period can be used in a design phase as a parameter to select the angle at which the pattern drop-off occurs, as shown in Fig. 8(a). When increasing the array unit cell dimensions, the AEP becomes more and more directive, with a redistribution of radiated power from the low-gain regions ($\theta < -\theta_{\text{drop}}$) to the rest of the field of view. From Fig. 8(b), it is apparent that the tilt angle is a convenient parameter to shape the gain levels in the suppressed angular region. As a result, the combination of the two parameters (d_x and α) can be conveniently used to effectively realize angular filtering by mean of array of stacked dipoles or patches. For comparison, Fig. 8(b) also shows the AEP when the elements are not tilted, to highlight how the tilt does not change the overall radiated power, but allows to redistribute it in the field of view by increasing the gain for positive scan angles while reducing it for negative scan angles.

D. Grating Lobe and Polarization Analysis

Since the asymmetry of the radiation pattern is achieved only for interelement distances higher than half wavelength, a grating lobe analysis is reported in this section. For example, Fig. 9 shows the grating lobe diagram for the array of tilted stacked dipoles, when the period is 0.6λ. We also plot a color map of the AEP as a function of the scan directions (k_{x0}, k_{y0}) in the circle with radius k_0 centered in the origin, representing the visible region. It is evident that, as the circles associated with the Floquet modes overlap, grating lobes can enter the visible region when scanning. For example, when the array scans to $\theta_{\text{scan}} = 50°$, the Floquet mode (m_x, m_y) equal to $(-1, 0)$ is within the visible region. However, this higher order Floquet wave corresponds to a direction for which the AEP is lower than -12 dB. To clarify this aspect, a pattern cut

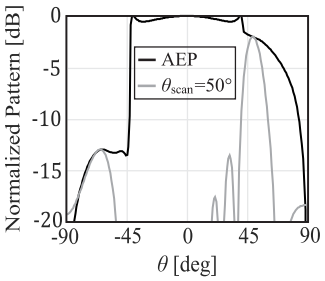

Fig. 10. AEP of an array of stacked dipoles with interelement distance 0.6λ and array pattern calculated by windowing technique for 10 elements, when scanning to 50°. Elements are tilted by $\alpha = 30°$.

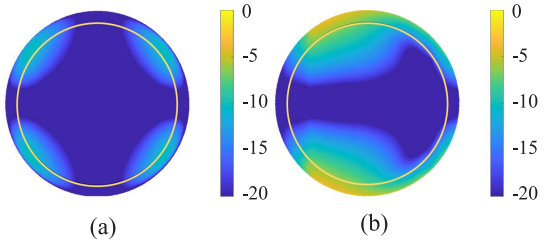

Fig. 11. Cross-polarized u–v pattern of an infinite array of stacked dipoles spaced 0.6λ_0 for (a) $\alpha = 0°$ and (b) $\alpha = 30°$. Yellow circles: scanning angle of 60°.

for $\phi = 0°$ is shown in Fig. 10, including the AEP as well as the array pattern for 10×10 elements, calculated with a windowing technique [21], [22]. A grating lobe points at $-65°$ but it is weighted by the element pattern, thus it remains -12 dB below the maximum. As a consequence, the gain of the main beam does not sensibly decrease with respect to the ideal $\cos\theta$ profile.

Fig. 11 shows u–v cross-polarized patterns of the unit cell shown in Fig. 5, for element tilt of $\alpha = 0°$ and $\alpha = 30°$. In the E-plane, the cross-pol is not affected by the tilt, since both the x- and the z- components of the current radiate copolar fields. However, in the H-plane or in diagonal planes, the X-pol increases due to the tilting. Within a scan range up to $\theta = 60°$ (indicated with a yellow inner circle in the plot), the worst X-pol is -6 dB for the tilted element, while it is -10 dB for the nontilted one.

IV. Finite Linear Array Analysis

To investigate the radiation properties of arrays comprising a finite number of elements, a spectral MoM for finite linear array of tilted stacked dipoles is also derived, to provide a simulation tool much faster than commercial solvers and to enable simulations of very large arrays. The method analyzes arrays of dipoles with arbitrarily tilt in the presence of a backing reflector. For efficient analysis of large arrays, we again consider only a single sinusoidal basis function for the longitudinal current on each dipole.

The geometry under analysis is depicted in Fig. 12, which shows the original array with the backing reflector and the equivalent problem obtained by applying the image theorem. The array consists in N_x stacked dipole elements in the presence of the ground plane, thus leading to $4N_x$ basis functions for the active and passive dipoles and their images. The mutual impedances are computed in different ways, depending on the pair of basis and test functions to be evaluated.

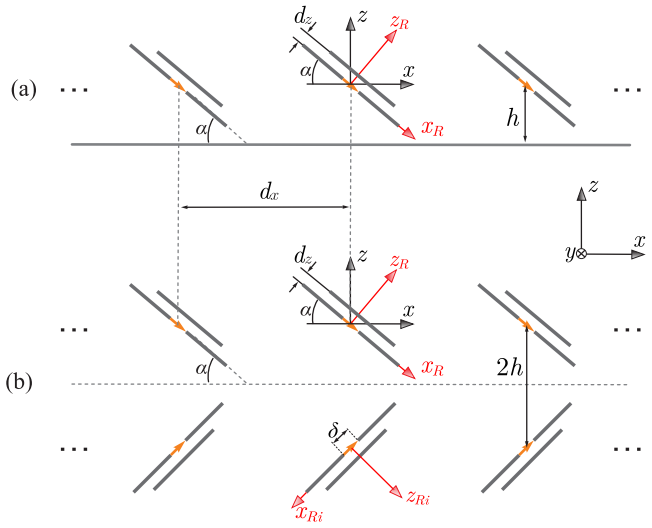

Fig. 12. Linear array of skewed stacked dipoles (a) above an infinite ground plane and (b) application of image theorem.

A. Mutual Impedance Computation

Let us consider any pair of parallel dipoles, for example, oriented along $\hat{\boldsymbol{x}}_R$, with indexes n and n', centered in the points $(x_{Rn}, 0, z_{Rn})$ and $(x_{Rn'}, 0, z_{Rn'})$, respectively. The mutual impedance can be written as a double spectral integral

$$Z_{nn'} = -\frac{1}{2\pi}\int_{-\infty}^{\infty} B_{l_{n'}}(k_{x_R}) B_{l_n}(-k_{x_R}) \cdot D_{nn'}(k_{x_R}) e^{-jk_{x_R}(x_{Rn}-x_{Rn'})} dk_{x_R} \quad (22)$$

where l_n and $l_{n'}$ are the length of the nth and n'th dipoles, respectively, and the function $D_{nn'}$ is given by

$$D_{nn'}(k_{x_R}) = \frac{1}{2\pi}\int_{-\infty}^{\infty} J_0(k_y w/2) G_{2D,x_R x_R}(k_{x_R}, k_y) \cdot e^{-j\sqrt{k_0 - k_{x_R}^2 - k_y^2}|z_{Rn}-z_{Rn'}|} dk_y . \quad (23)$$

The expressions in (22) and (23) are obtained by considering Galerkin projection for the x_R-oriented distribution, while assuming point matching for the y- and z_R-variables. This choice is made so that, when computing the self-impedance, for which $z_{Rn} = z_{Rn'}$, the integral in (23) can be solved rigorously in closed form as done in [13], thus only a single spectral integral in the variable k_{x_R} remains to be evaluated. When the distance between dipoles is much larger than the dipole width ($|z_{Rn} - z_{Rn'}| \gg w$), (23) can also be approximately solved analytically, as shown in [23]. For distances $|z_{Rn} - z_{Rn'}|$ in the order of w, we solve numerically the double integral, by pretabulating the function $D_{nn'}$ for a set of k_{x_R} points and using a cubic interpolation to fit the function through these points. Alternatively, one can use the closed form expressions for the self-impedance and mutual impedance from [19] and [26], which assume infinitely thin dipoles. These expressions are accurate for sufficiently large distance between dipoles and for very small dipole width. However, when the dipole width and the distances are in the order of $\lambda/10$, the expressions in (22) and (23) provide better accuracy, since they account for the transverse distribution of the current on the strips.

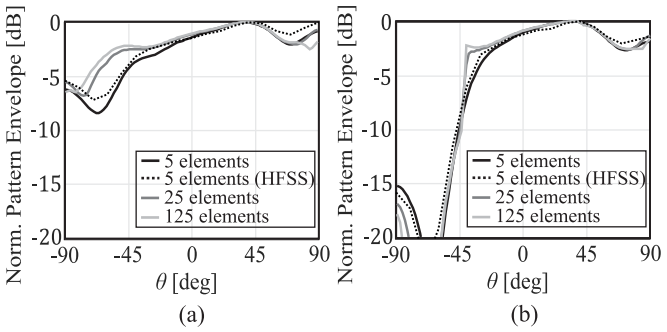

Fig. 13. Pattern envelope as a function of the number of elements for a linear array of stacked dipoles in the presence of a backing reflector. The inclination angle is $\alpha = 30°$ and the distance between elements is (a) $d_x = 0.5\lambda$ and (b) $d_x = 0.6\lambda$.

The mutual impedance between dipoles that are not parallel (any real dipole with any image) is calculated analytically using the method described in [27], which is valid for skewed dipoles with arbitrary length and distance. Moreover, for equal tilt of all the elements, the MoM matrix is block Toeplitz, thus a reduced set of the impedance terms needs to be calculated.

B. Radiation Properties

Based on the described efficient MoM, a parametric analysis on the radiation pattern of the finite array is carried out, varying the interelement distance d_x, the angle of inclination α, and the number of elements N_x. The geometrical dimensions for the stacked dipole element are the same as in Section III-B.

Fig. 13 reports the normalized envelop of the array radiation pattern as a function of the scan angle, for two different array periods and for various array sizes. The envelope of a 5-element linear array simulated with HFSS is also included to verify the MoM solution. It is apparent that, when the distance between elements is half wavelength [Fig. 13(a)], a small pattern asymmetry is obtained for small arrays, but such asymmetry tends to disappear when increasing the number of elements. This observation is in line with infinite array results. The curves shown in Fig. 13(b) exhibit a very different behavior for array periods larger than $\lambda/2$, for which the asymmetry remains nearly constant and independent on the number of elements. We can also note that, since the array is 1-D and located on an infinite ground plane, the gain for positive scan angles does not follow the $\cos\theta$ typical of doubly periodic array, thus it does not drop to 0 even for scanning close to 90°. This behavior is typical of linear arrays, where a proper phase shift between the elements can still produce high gain in the endfire direction [19].

Fig. 14 shows the normalized E-plane pattern for an array of 25 elements with different periods and inclination angles of $\alpha = 30°$. As for the infinite array case, the angular position of the gain drop can be controlled with the array period. However, unlike the infinite array, even for $d_x = 0.5\lambda$, a 25-element linear array can achieve a certain degree of asymmetry. The tilt angle influences both the gain levels in low-radiation angular region and for wide positive angles [Fig. 14(b)].

Fig. 8(a) or Fig. 14(a) also illustrates the frequency dependence of the proposed concept. For a given array spacing, changing the frequency causes a shift of the angle at which

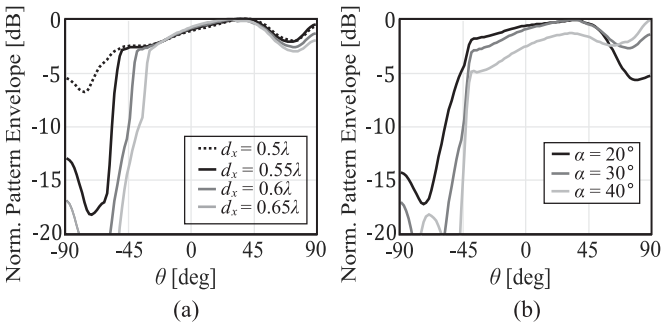

Fig. 14. Pattern envelope of a linear array of 25 stacked dipoles (a) tilted 30° for different spacings d_x and (b) with an interelement distance of 0.6λ for different tilt angles α.

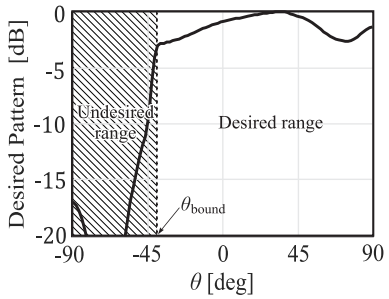

Fig. 15. Definition of desired and undesired angular ranges, bounded by the direction θ_{bound}.

the gain drops. To quantify the effect of this shift on the performance and to provide guidelines for array designs, we define in Section IV-C a figure of merit to assess the asymmetry.

C. Design Guidelines

We can imagine to divide the field of view in two angular regions, as in Fig. 15: the 'desired range' refers to the angles for which a high and stable gain is wished for, whereas the 'undesired range' is where suppression of gain is intended. These two regions are limited by the angle θ_{bound}. To quantify the asymmetry of the pattern, we define a figure of merit (A) that we refer to as an asymmetry factor

$$A(\theta_{bound}) = 1 - \frac{P(-90^\circ < \theta < \theta_{bound})}{P(\theta_{bound} < \theta < 90^\circ)} \frac{90^\circ - \theta_{bound}}{\theta_{bound} + 90^\circ} \quad (24)$$

where $P(\theta_1 < \theta < \theta_2)$ is the power contained between the angles θ_1 and θ_2. The term $(90^\circ - \theta_{bound})/(\theta_{bound} + 90^\circ)$ has been included in (24) to compensate for the difference in power ratio while varying θ_{bound}. To clarify this aspect, let us consider an ideal radiation pattern, equal to 1 in the desired range and 0.1 in the undesired range. If we calculate the figure of merit A removing the ratio $(90^\circ - \theta_{bound})/(\theta_{bound} + 90^\circ)$, the resulting values will depend on θ_{bound}: e.g., $A(-80^\circ) = 1 - (0.1 \times 10^\circ)/(1 \times 170^\circ) = 0.994$, $A(-45^\circ) = 1 - (0.1 \times 45^\circ)/(1 \times 135^\circ) = 0.967$, $A(0^\circ) = 1 - (0.1 \times 90^\circ)/(1 \times 90^\circ) = 0.9$. On the other hand, adding the term $(90^\circ - \theta_{bound})/(\theta_{bound} + 90^\circ)$ gives the same asymmetry factor in all cases ($A(-80^\circ) = A(-45^\circ) = A(0^\circ) = 0.9$), which depends only on the values of the radiation pattern in the desired and undesired regions.

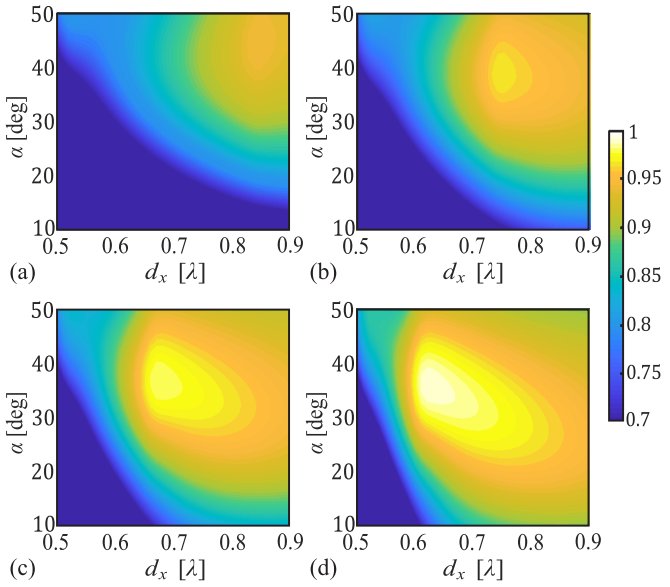

Fig. 16. Asymmetry of the radiation pattern (in decibels) varying the inclination angle and interelement distance for θ_{bound} equal to (a) -10°, (b) -20°, (c) -30°, and (d) -40°.

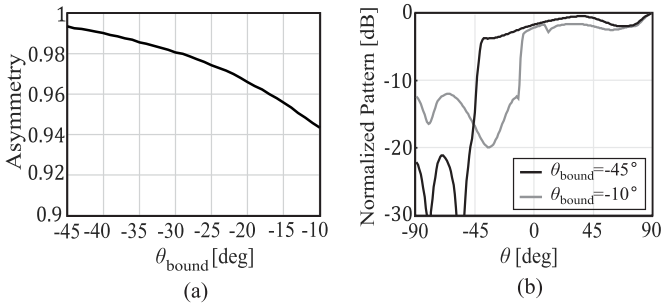

Fig. 17. (a) Maximum value of the asymmetry factor when varying θ_{bound} and (b) normalized array pattern envelopes for $\theta_{bound} = -45^\circ$ and $\theta_{bound} = -10^\circ$.

Fig. 16 shows a map of the asymmetry (normalized to the maximum) for different θ_{bound} (-10°, -20°, -30° and -40°) while varying the interelement distance and the inclination angle. An array of 25 elements is considered. Depending on the specified θ_{bound}, the optimal configuration to achieve maximum asymmetry occurs for different d_x and α.

Fig. 17(a) shows the maximum of the asymmetry while varying θ_{bound}. The decreasing values can be explained by observing the array pattern envelopes for $\theta_{bound} = -45^\circ$ and $\theta_{bound} = -10^\circ$, in Fig. 17(b). The side lobes in the undesired region are higher for larger periods, which explain the decrease in the asymmetry factor. The values of inclination angle and interelement spacing correspondent to the maxima of the asymmetry factor are plotted versus θ_{bound} in Fig. 18. The value of d_x that yields the maximum increases with θ_{bound} and also corresponds to the value that gives $\theta_{drop} = \theta_{bound}$ calculated from (21). The tilt angle that gives maximum asymmetry is also changing with θ_{bound}. An interpretation of this behavior can be related to the mutual blockage effects between array elements that limits the maximum tilt angle for small periods, as depicted in the inset of Fig. 18.

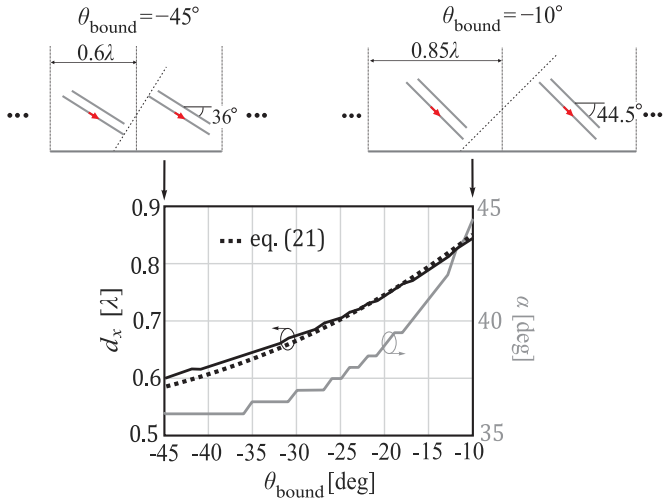

Fig. 18. Interelement distance and inclination angle corresponding to maximum asymmetry for different θ_{bound}.

V. Conclusion

We presented an analysis of infinite and finite arrays with tilted elements, with particular focus on their radiation characteristics. A periodic MoM was developed to analyze different dipole geometries through analytical expressions. It was shown that skewed stacked dipole elements can be used to achieve nonsymmetric radiation when used in combination with a backing reflector, for interelement spacings larger than half wavelength. The dependence of the AEP on the inclination of the elements and the array period was discussed. These two parameters can be varied to control the pattern profile, thus the proposed elements can be effectively employed to implement pattern shaping.

Finite linear arrays of stacked dipoles were also investigated. The analysis was based on an efficient MoM approach, based on entire domain basis functions, where several mutual coupling terms were analytically computed. The finite array analysis allowed to highlight the dependence of the pattern asymmetry on the number of elements, besides the spacing and tilt angle.

Appendix A
Fourier Transform of the Current Distribution

The 3-D Fourier transform of the current in (9) can be written as

$$\begin{aligned} J(k_x,k_y,k_z) &= \iiint j(x,y,z)e^{jk_xx}e^{jk_yy}e^{jk_zz}dxdydz \\ &= i_0\iiint_V b_l(x\cos\alpha - z\sin\alpha)e(y)\delta(x\sin\alpha + z\cos\alpha)\cdot \\ &\quad e^{jk_xx}e^{jk_yy}e^{jk_zz}dxdydz \end{aligned} \tag{25}$$

where V is a volume containing the entire dipole. The integral along y yields the Bessel function of the zeroth order. Therefore, the Fourier transform is expressed as a double integral along x and y

$$J(k_x,k_y,k_z) = i_0J_0\left(\frac{k_yw}{2}\right)\iint_A b_l(x\cos\alpha - z\sin\alpha)\cdot \delta(x\sin\alpha + z\cos\alpha)e^{jk_xx}e^{jk_zz}dxdz \tag{26}$$

where A is the surface of the dipole. We can apply the change of variables

$$x' = x\cos\alpha - z\sin\alpha, \quad z' = x\sin\alpha + z\cos\alpha \tag{27}$$

where the Jacobian of the transformation equals unity

$$\det\begin{vmatrix} dx'/dx & dx'/dz \\ dz'/dx & dz'/dz \end{vmatrix} = \det\begin{vmatrix} \cos\alpha & -\sin\alpha \\ \sin\alpha & \cos\alpha \end{vmatrix} = 1\,. \tag{28}$$

The expression in (26) becomes

$$J(k_x,k_y,k_z) = i_0J_0\left(\frac{k_{ym}w}{2}\right)\iint_A b_l(x')\delta(z')\cdot e^{j(k_x\cos\alpha - k_z\sin\alpha)x'}e^{j(k_x\sin\alpha + k_z\cos\alpha)z'}dx'dz'\,. \tag{29}$$

Closing the integral in x' and z' we can find the final expression for the spectral current

$$J(k_x,k_y,k_z) = i_0J_0\left(\frac{k_{ym}w}{2}\right)B_l(k_x\cos\alpha - k_z\sin\alpha)\,. \tag{30}$$

Appendix B
Closed-Form Solution of the Active Input Impedance

The active input impedance in (13) contains a spectral integral in the k_z-variable

$$I = \int_{-\infty}^{\infty} B_l^2(k_{x_R})G_{x_Rx_R}(k_{xm},k_{ym},k_z)dk_z. \tag{31}$$

The argument of the integral comprises a product between the spectral-domain piecewise sinusoidal distributions defined in (11). When writing explicitly this product, we obtain, after a few algebraic steps

$$B_l^2(k_{x_R}) = \left(\frac{2k_0}{\sin(k_0l/2)}\right)^2\frac{A_1 + A_2(k_{xm},k_z) + A_3(k_{xm},k_z)}{\left(k_0^2 - k_{x_R}^2\right)^2} \tag{32}$$

where

$$\begin{aligned} A_1 &= \frac{1}{2} + \cos^2(k_0l/2) \\ A_2(k_{xm},k_z) &= \frac{e^{jk_{x_R}l}}{4} - \cos(k_0l/2)e^{jk_{x_R}l/2} \\ A_3(k_{xm},k_z) &= \frac{e^{-jk_{x_R}l}}{4} - \cos(k_0l/2)e^{-jk_{x_R}l/2}\,. \end{aligned} \tag{33}$$

The components of the free-space dyadic spectral Green's function used in (31) can be expressed as

$$G_{xx}^{ej}(k_x,k_y,k_z) = j\frac{\zeta}{k_0}\frac{k_0^2-k_x^2}{k_0^2-k_x^2-k_y^2-k_z^2}$$
$$G_{xz}^{ej}(k_x,k_y,k_z) = j\frac{\zeta}{k_0}\frac{-k_xk_z}{k_0^2-k_x^2-k_y^2-k_z^2}$$
$$G_{zz}^{ej}(k_x,k_y,k_z) = j\frac{\zeta}{k_0}\frac{k_0^2-k_z^2}{k_0^2-k_x^2-k_y^2-k_z^2}. \quad (34)$$

Substituting all the components in the definition $G_{x_Rx_R} = G_{xx}\cos^2\alpha - 2\,G_{xz}\sin\alpha\cos\alpha + G_{zz}\sin^2\alpha$ leads to

$$G_{x_Rx_R}(k_{xm},k_{ym},k_z) = j\frac{\zeta_0}{k_0}\frac{k_0^2-(k_{xm}\cos\alpha-k_z\sin\alpha)^2}{k_0^2-k_{xm}^2-k_{ym}^2-k_z^2}. \quad (35)$$

By combining (32) and (35), we can write the integral as

$$I = j\frac{\zeta_0}{k_0}\left(\frac{2k_0}{\sin(k_0l/2)}\right)^2\int_{-\infty}^{\infty}\frac{1}{k_0^2-k_{xm}^2-k_{ym}^2-k_z^2}\cdot \frac{A_1+A_2(k_{xm},k_z)+A_3(k_{xm},k_z)}{k_0^2-(k_{xm}\cos\alpha-k_z\sin\alpha)^2}dk_z \quad (36)$$

The integrand in (36) contains four poles

$$k_{zp1} = k_{xm}\cot\alpha + k_0\csc\alpha$$
$$k_{zp2} = k_{xm}\cot\alpha - k_0\csc\alpha$$
$$k_{zp3} = -\sqrt{k_0^2-k_{xm}^2-k_{ym}^2}$$
$$k_{zp4} = \sqrt{k_0^2-k_{xm}^2-k_{ym}^2}. \quad (37)$$

The location of these poles in the complex plane can change depending on the Floquet mode indexes, the scan angles, and the tilt of the dipoles. For instance, when considering the fundamental Floquet mode ($m_x = m_y = 0$) and scanning to broadside with a tilt of $\alpha = 30°$, the poles are located on the real axis as shown in Fig. 19(a). For the mode $m_x = -1, m_y = 0$, the poles move in the configuration depicted in Fig. 19(b).

The integral in (36) can then be written in terms of the polar singularities as

$$I = j\frac{\zeta_0}{k_0}\left(\frac{2k_0}{\sin(k_0l/2)}\right)^2\cdot \int_{-\infty}^{\infty}(A_1+A_2(k_{xm},k_z)+A_3(k_{xm},k_z))\prod_{i=1}^{4}\frac{1}{k_z-k_{zpi}}dk_z. \quad (38)$$

By using the Cauchy theorem, the residue theorem can be applied. To ensure convergence, the integral can be split in three contributions: the path can be deformed at infinity as in Fig. 19(c) for the terms A_1 and A_2, whereas the deformation shown in Fig. 19(d) is considered for A_3. For each of the three contributions, the result of the integral can be obtained as the sum of the residues correspondent to the polar singularities that are enclosed in the pertaining deformation path, where the sign of the residues change if the path is clockwise or counterclockwise.

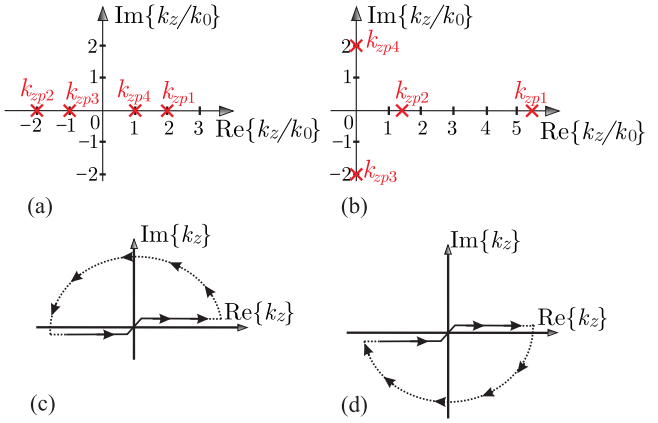

Fig. 19. Locations of the poles scanning at broadside with a tilt of $\alpha = 30°$ considering (a) fundamental Floquet mode and (b) e $m_x = -1, m_y = 0$. The deformation paths used depending on the convergence of the contributions. (c) Upward. (d) Downward.

APPENDIX C
SYMMETRY PROPERTIES OF IMPEDANCE

In this section, a proof of the symmetry property of the active input impedance is reported. To simplify the problem, we consider the expression in (13), associated with an infinite tilted dipole array in free space. However, the same steps can be followed for all other cases. If we consider only the fundamental Floquet mode in (13) and scan to $\theta = \theta_0$, the active input impedance is

$$Z_{\text{in,fs}}|_{m_x=m_y=0,\theta=\theta_0} = \frac{-1}{2\pi d_xd_y}j\frac{\zeta_0}{k_0}J_0^2\left(\frac{k_{y0}w}{2}\right)\cdot \int_{-\infty}^{\infty}B_l^2(k_{x0}\cos\alpha-k_z\sin\alpha)\frac{k_0^2-(k_{x0}\cos\alpha-k_z\sin\alpha)^2}{k_0^2-k_{x0}^2-k_{y0}^2-k_z^2}dk_z. \quad (39)$$

When scanning in the specular direction $\theta = -\theta_0$, k_{x0} and k_{y0} change sign and if we apply the change of variable $k_z = -k'_z$, we obtain

$$Z_{\text{in,fs}}|_{m_x=m_y=0,\theta=-\theta_0} = \frac{-1}{2\pi d_xd_y}j\frac{\zeta_0}{k_0}J_0^2\left(-\frac{k_{y0}w}{2}\right)\cdot\int_{-\infty}^{\infty}B_l^2(k'_z\sin\alpha-k_{x0}\cos\alpha)\cdot\frac{k_0^2-(k'_z\sin\alpha-k_{x0}\cos\alpha)^2}{k_0^2-k_{x0}^2-k_z'^2}dk'_z. \quad (40)$$

It is evident that (39) and (40) are identical, since the current spectrum is an even function, i.e., $B_l(k) = B_l(-k)$ and $J_0(k) = J_0(-k)$. Similar steps can be followed to demonstrate the impedance symmetry for the higher order modes. In this

case, the scan impedance for $\theta = \theta_0$ is

$$Z_{\text{in,fs}}|_{\theta=\theta_0} = \frac{-1}{2\pi d_x d_y} j\frac{\zeta_0}{k_0} \sum_{m_x=-\infty}^{\infty} \sum_{m_y=-\infty}^{\infty} J_0^2\left(\frac{\left(k_{y0}-\frac{2\pi m_y}{d_y}\right)w}{2}\right) \int_{-\infty}^{\infty} B_l^2\left(\left(k_{x0}-\frac{2\pi m_x}{d_x}\right)\cos\alpha - k_z \sin\alpha\right) \cdot \frac{k_0^2 - \left(\left(k_{x0}-\frac{2\pi m_x}{d_x}\right)\cos\alpha - k_z\sin\alpha\right)^2}{k_0^2 - \left(k_{x0}-\frac{2\pi m_x}{d_x}\right)^2 - \left(k_{y0}-\frac{2\pi m_y}{d_y}\right)^2 - k_z^2} dk_z. \quad (41)$$

For $\theta = -\theta_0$, by applying the change of variable $k_z = -k'_z$, $m_x = -m'_x$, and $m_y = -m'_y$, we obtain the same expression for the impedance: $Z_{\text{in,fs}}|_{\theta=\theta_0} = Z_{\text{in,fs}}|_{\theta=-\theta_0}$. This result is consistent with the symmetry property of the active reflection coefficient [28], which is demonstrated in [5] and [6], for periodic and reciprocal problems.

REFERENCES

[1] A. Catalani, F. Di Paolo, M. Migliorelli, L. Russo, G. Toso, and P. Angeletti, "Ku band hemispherical fully electronic antenna for aircraft in flight entertainment," *Int. J. Antennas Propag.*, vol. 2009, Mar. 2009, Art. no. 230650. doi: 10.1155/2009/230650.

[2] R. J. Bolt *et al.*, "Characterization of a dual-polarized connected-dipole array for Ku-band mobile terminals," *IEEE Trans. Antennas Propag.*, vol. 64, no. 2, pp. 591–598, Feb. 2016.

[3] F. Tiezzi, D. Llorens, C. Dominguez, and M. Fajardo, "A compact Ku-band transmit/receive low-profile antenna for broadband mobile satellite communications," in *Proc. 4th Eur. Conf. Antennas Propag. (EuCAP)*, Barcelona, Spain, Apr. 2010, pp. 1–4.

[4] J. Biosca, D. Llorens, and M. C. Viganó, "Side-lobe reduction with overlapped beam-forming network for Ku-band hybrid antenna array," in *Proc. 10th Eur. Conf. Antennas Propag.*, Davos, Switzerland, Apr. 2016, pp. 1–5.

[5] A. K. Bhattacharyya, "Active element pattern symmetry for asymmetrical element arrays," *IEEE Antennas Wireless Propag. Lett.*, vol. 6, pp. 275–278, 2007.

[6] H. Steyskal, "On the merit of asymmetric phased array elements," *IEEE Trans. Antennas Propag.*, vol. 61, no. 7, pp. 3519–3524, Jul. 2013.

[7] R. Hyneman, "A technique for the synthesis of line-source antenna patterns having specified sidelobe behavior," *IEEE Trans. Antennas Propag.*, vol. AP-16, no. 4, pp. 430–435, Jul. 1968.

[8] R. Elliott, "Design of line source antennas for narrow beamwidth and asymmetric low sidelobes," *IEEE Trans. Antennas Propag.*, vol. 23, no. 1, pp. 100–107, Jan. 1975.

[9] L. Shafai, "Scan gain enhancement in phased arrays by element pattern synthesis," in *Proc. 7th Int. Conf. Antennas Propag. (ICAP)*, vol. 2, Apr. 1991, pp. 914–917.

[10] C. J. Sletten, P. Blacksmith, Jr., and G. Forbes, Jr., "New method of antennas array synthesis applied to generation of double-step patterns," *IRE Trans. Antennas Propag.*, vol. 5, no. 4, pp. 369–373, Oct. 1957.

[11] A. H. Hussein, H. H. Abdullah, A. M. Salem, S. Khamis, and M. Nasr, "Optimum design of linear antenna arrays using a hybrid MoM/GA algorithm," *IEEE Antennas Wireless Propag. Lett.*, vol. 10, pp. 1232–1235, 2011.

[12] D. Hua, W. Wu, and D.-G. Fang, "Linear array synthesis to obtain broadside and endfire beam patterns using element-level pattern diversity," *IEEE Trans. Antennas Propag.*, vol. 65, no. 6, pp. 2992–3004, Jun. 2017.

[13] A. Neto and S. Maci, "Green's function for an infinite slot printed between two homogeneous dielectrics. I. Magnetic currents," *IEEE Trans. Antennas Propag.*, vol. 51, no. 7, pp. 1572–1581, Jul. 2003.

[14] M. Kominami, D. M. Pozar, and D. H. Schaubert, "Dipole and slot elements and arrays on semi-infinite substrates," *IEEE Trans. Antennas Propag.*, vol. AP-33, no. 6, pp. 600–607, Jun. 1985.

[15] D.-H. Kwon and D. M. Pozar, "Energy storage and radiation Q of infinite planar dipole phased arrays," *IEEE Trans. Antennas Propag.*, vol. 62, no. 1, pp. 153–162, Jan. 2014.

[16] C.-H. Tsao and R. Mittra, "Spectral-domain analysis of frequency selective surfaces comprised of periodic arrays of cross dipoles and Jerusalem crosses," *IEEE Trans. Antennas Propag.*, vol. AP-32, no. 5, pp. 478–486, May 1984.

[17] R. F. Harrington, *Field Computation by Moment Methods*. Piscataway, NJ, USA: IEEE Press, 1993.

[18] R. C. Hansen, *Phased Array Antennas*. New York, NY, USA: Wiley, 2001.

[19] C. A. Balanis, *Antenna Theory: Analysis and Design*, 3rd ed. Hoboken, NJ, USA: Wiley, 2005.

[20] A. Clemente, M. Pigeon, L. Rudant, and C. Delaveaud, "Design of a super directive four-element compact antenna array using spherical wave expansion," *IEEE Trans. Antennas Propag.*, vol. 63, no. 11, pp. 4715–4722, Nov. 2015.

[21] A. Ishimaru, R. Coe, G. Miller, and W. Geren, "Finite periodic structure approach to large scanning array problems," *IEEE Trans. Antennas Propag.*, vol. AP-33, no. 11, pp. 1213–1220, Nov. 1985.

[22] A. K. Skrivervik and J. R. Mosig, "Analysis of finite phase arrays of microstrip patches," *IEEE Trans. Antennas Propag.*, vol. 41, no. 8, pp. 1105–1114, Aug. 1993.

[23] D. Cavallo, "Connected array antennas: Analysis and design," Ph.D. Dissertation, Dept. Elect. Eng., Eindhoven Univ. Technol., Eindhoven, The Netherlands, Nov. 2011.

[24] H. King, "Mutual impedance of unequal length antennas in echelon," *IRE Trans. Antennas Propag.*, vol. 5, no. 3, pp. 306–313, Jul. 1957.

[25] R. W. P. King, R. B. Mack, and S. S. Sandler, *Arrays of Cylindrical Dipoles*. Cambridge, U.K.: Cambridge Univ. Press, 1968, ch. 7.

[26] R. W. P. King, G. J. Fikioris, and R. B. Mack, *Cylindrical Antennas and Arrays*. Cambridge, U.K.: Cambridge Univ. Press, 2002, ch. 7.

[27] J. H. Richmond and N. Geary, "Mutual impedance of nonplanar-skew sinusoidal dipoles," *IEEE Trans. Antennas Propag.*, vol. AP-23, no. 3, pp. 412–414, May 1975.

[28] D. M. Pozar, "The active element pattern," *IEEE Trans. Antennas Propag.*, vol. 42, no. 8, pp. 1176–1178, Sep. 1994.

Cristina Yepes (S'17) received the M.Sc. degree in telecommunication engineering from the University of Navarra, Navarra, Spain, in 2015. She is currently pursuing the Ph.D. degree with the Terahertz Sensing Group, Delft University of Technology, Delft, The Netherlands, and with the Radar Department, Netherlands Organization for Applied Scientific Research (TNO) Defense, Safety and Security, The Hague, The Netherlands.

Her current research interests include analysis and design techniques for phased array antennas and frequency-selective surfaces, and analytical and numerical methods for antenna characterization.

Dr. Yepes was a co-recipient of the Best Innovative Paper Prize at the 39th ESA Antenna Workshop in 2018.

Erio Gandini (M'17) received the M.Sc. degree in electrical engineering from the University of Modena and Reggio Emilia, Modena, Italy, in 2009 and the Ph.D. degree in electrical engineering from the University of Rennes 1, Rennes, France, in 2012.

In 2011, he was a Visiting Ph.D. Student with the University of Michigan, Ann Arbor, MI, USA. In 2013, he joined the Ecole Polytechnique Fédérale de Lausanne, Lausanne, Switzerland, as a Post-Doctoral Researcher. From 2013 to 2017, he was a Post-Doctoral Researcher with the Delft University of Technology, Delft, The Netherlands. Since 2016, he has been a Microwave and Antenna Scientist with the Radar Department, Netherlands Organization for Applied Scientific Research (TNO) Defense, Safety, and Security, The Hague, The Netherlands. He has authored and coauthored more than 55 scientific publications in peer-reviewed international journals and conference proceedings. His current research interests include the analysis and design of phased array antennas, quasi-optical systems, submillimeter and terahertz imaging systems, frequency-selective surfaces, and beam-forming networks.

Dr. Gandini was a recipient of the NEWFOCUS Grant in 2011 for Integrated Metamaterial-Based Focusing Systems for Antenna Beamformers Project and the honorable mention at the Student Paper Competition at the International Microwave Symposium (IMS) 2012. He was also a co-recipient of the Best Innovative Paper Prize at the 39th ESA Antenna Workshop in 2018.

Stefania Monni (S'01–M'06–SM'18) received the M.Sc. degree *(summa cum laude)* in electronic engineering from the University of Cagliari, Cagliari, Italy, in 1999 and the Ph.D. degree in electronic engineering from the Technical University of Eindhoven, Eindhoven, The Netherlands, in 2005. From 2001 to 2005, she carried out her Ph.D. research at the Radar Technology Department, Netherlands Organization for Applied Scientific Research (TNO), The Hague, The Netherlands.

From 1999 to 2000, she was an Undergraduate and a Graduate Trainee with the Radio Frequency System Division, European Space Research and Technology Center (ESA-ESTEC), Noordwijk, The Netherlands. She is currently a Senior Scientist and Leader of the Antenna Team, TNO. Her current research interests include analysis and design techniques for phased array antennas and frequency-selective surfaces, wideband antennas, and digital beam forming for active and passive radars.

Dr. Monni will be an Elected Member of the EurAAP Board of Directors from January 2020. She was a co-recipient of the Best Innovative Paper Prize at the 39th ESA Antenna Workshop in 2018. She is currently the Benelux Delegate at the European Association on Antennas and Propagation (EurAAP). She is a Co-Organizer and the Co-Chair of several special sessions and technical committee member at international conferences. She serves as a Reviewer for the IEEE ANTENNAS AND WIRELESS PROPAGATION LETTERS (AWPL), the PROCEEDINGS OF THE IEEE, the IEEE TRANSACTIONS ON ANTENNAS AND PROPAGATION (TAP), and the IEEE TRANSACTIONS ON GEOSCIENCE AND REMOTE SENSING (TGRS).

Andrea Neto (M'00–SM'10–F'16) received the Laurea degree *(summa cum laude)* in electronic engineering from the University of Florence, Florence, Italy, in 1994 and the joint Ph.D. degree in electromagnetics from the University of Siena, Siena, Italy, and the European Space Agency Research and Technology Center, Noordwijk, The Netherlands, in 2000.

From 2000 to 2001, he was a Post-Doctoral Researcher with the Sub-Millimeter-Wave Advanced Technology Group, California Institute of Technology, Pasadena, CA, USA. From 2002 to 2010, he was a Senior Antenna Scientist with TNO Defense, Security, and Safety, The Hague, The Netherlands. In 2010, he became a Full Professor of applied electromagnetism with the Electrical Engineering, Mathematics and Computer Science Department, Delft University of Technology, Delft, The Netherlands, where he formed and currently leads the Terahertz (THz) Sensing Group. His current research interests include the analysis and design of antennas with an emphasis on arrays, dielectric lens antennas, wideband antennas, electromagnetic bandgap structures, and THz antennas.

Dr. Neto is a member of the Technical Board of the European School of Antennas and a member of the steering committee of the network of excellence NEWFOCUS, dedicated to focusing techniques in mm-wave and sub-mm-wave regimes. He was a co-recipient of the H. A. Wheeler Award for the best applications paper of the year 2008 in the IEEE TRANSACTIONS ON ANTENNAS AND PROPAGATION, the Best Innovative Paper Prize at the 30th ESA Antenna Workshop in 2008, the Best Antenna Theory Paper Prize at the European Conference on Antennas and Propagation in 2010, and the European Research Council Starting Grant in 2011 to perform research on Advanced Antenna Architectures for THz Sensing Systems. He is an Organizer of the course on Antenna Imaging Techniques, European School of Antennas (ESoA). He was the Awards and Grants Chair of the European Conference on Antennas and Propagation in 2014. He served as an Associate Editor for the IEEE TRANSACTIONS ON ANTENNAS AND PROPAGATION from 2008 to 2013 and IEEE ANTENNAS AND WIRELESS PROPAGATION LETTERS from 2005 to 2013. He currently serves as an Associate Editor for the IEEE TRANSACTIONS ON TERAHERTZ SCIENCE AND TECHNOLOGY.

Frank E. van Vliet (M'96–SM'06) received the M.Sc. (Hons.) and Ph.D. degrees in electrical engineering, with a focus on monolithic microwave integrated circuit (MMIC) filters, from the Delft University of Technology, Delft, The Netherlands, in 1992 and 1997, respectively.

In 1997, he joined Netherlands Organization for Applied Scientific Research (TNO), The Hague, The Netherlands, where he is currently a Principal Scientist responsible for MMIC, antenna, and transmit/receive module research. In 2007, he joined the Integrated Circuit Design Group, University of Twente, Enschede, The Netherlands, as a Professor in microwave integration, where he founded the Center for Array Technology. He has authored or coauthored more than 100 peer-reviewed publications. His current research interests include MMICs in all their aspects, advanced measurement techniques, and phased-array technology.

Dr. van Vliet is a member of the European Space Agencies Component Technology Board for Microwave Components and the European Defense Agencies CapTech IAP-01, and he serves as the Chair of the 2012 European Microwave Integrated Circuit Conference. He founded the Doctoral School of Microwaves and serves on the Technical Program Committee of EuMIC, the IEEE International Symposium on Phased Array Systems and Technology, the IEEE Compound Semiconductor IC Symposium, and the IEEE Conference on Microwaves, Communications, Antennas and Electronic Systems. He served as the Guest Editor for the IEEE MTT 2013 Special Issue on Phased-Array Technology.

Daniele Cavallo (S'09–M'11–SM'19) received the M.Sc. degree *(summa cum laude)* in telecommunication engineering from the University of Sannio, Benevento, Italy, in 2007, and the Ph.D. degree *(cum laude)* in electromagnetics from Eindhoven University of Technology (TU/e), Eindhoven, The Netherlands, in 2011.

From 2007 to 2011, he was with the Antenna Group, Netherlands Organization for Applied Scientific Research (TNO), The Hague, The Netherlands. From 2012 to 2015, he was a Post-Doctoral Researcher with the Microelectronics Department, Delft University of Technology (TU Delft), Delft, The Netherlands. In 2015, he joined the Chalmers University of Technology, Gothenburg, Sweden, as a Visiting Researcher. He is currently an Assistant Professor with the Terahertz Sensing Group, TU Delft. He has authored or coauthored around 130 articles published in peer-reviewed international journals and conference proceedings. His current research interests include analytical and numerical methods for antenna characterization, the design of antenna arrays, and on-chip antennas.

Dr. Cavallo is a member of the European Association on Antennas and Propagation (EurAAP) and a Co-Coordinator of the EurAAP working group—Active Array Antennas. He was a recipient of the Best Innovative Paper Prize at the 30th ESA Antenna Workshop in 2008, the Best Paper Award in Electromagnetics and Antenna Theory at the 11th European Conference on Antennas and Propagation (EuCAP) in 2017, and the Three-Year Personal Grant from the Netherlands Organization for Scientific Research (NWO VENI, 250 keuro), for developing Efficient On-Chip Antennas for Terahertz Applications. His students received the Best Student Paper Award at EuCAP 2013, the Special Mention at EuCAP 2015, and the Else Kooi Prize in 2016. He is currently an Associate Editor of the IEEE TRANSACTIONS ON ANTENNAS AND PROPAGATION.